Advances in Water Resources 96 (2016) 170–179

Contents lists available at ScienceDirect

Advances in Water Resources

journal homepage: www.elsevier.com/locate/advwatres

Field-wide flow simulation in fractured porous media within lattice Boltzmann framework

Z. Benamram, A. Tarakanov, H. Nasrabadi*, E. Gildin*

Texas A&M University, Harold Vance Department of Petroleum Engineering, 3116 TAMU College Station, TX 77843-3116, United States

ARTICLE INFO

Article history:
Received 10 February 2016
Revised 5 July 2016
Accepted 6 July 2016
Available online 20 July 2016

Keywords:
Lattice Boltzmann
Fracture simulation
Dimensional analysis
Generalized Navier Stokes
Reservoir simulation

ABSTRACT

In this paper, a generalized lattice Boltzmann model for simulating fluid flow in porous media at the representative volume element scale is extended towards applications of hydraulically and naturally fractured reservoirs. The key element within the model is the development of boundary conditions for a vertical well and horizontal fracture with minimal node usage. In addition, the governing non-dimensional equations are derived and a new set of dimensionless numbers are presented for the simulation of a fractured reservoir system. Homogenous and heterogeneous vertical well and fracture systems are simulated and verified against commercial reservoir simulation suites. Results are in excellent agreement to analytical and finite difference solutions.

1. Introduction

This paper will provide a numerical methodology for the simulation of fluid flow through a fractured reservoir system (FRS); the goal of which is to optimize fluid production while reducing the cost associated with improper characterization of the subsurface environment. We will focus on two aspects of the FRS considered most pivotal: first, the complex boundary geometries present within the FRS between the fracture and surrounding porous medium, and second, the various flow regimes present within the FRS at various scales.

The FRS, distinct from the porous rock matrix, provides high conductive pathways for fluid flow. The majority of fluid production comes from these high conductive pathways and the neighboring porous matrix, and so, the geometry of the FRS is a primary indicator of future fluid production (King, 2016, Warpinski and Teufel, 2016). The rate of production is also heavily dependent on the accelerating elements within the flow field. In a reservoir where fluid flows only through the porous rock matrix, Darcy flow is the primary flow regime (Dake, 1978). However, in the FRS, inertial flows and nonlinear damping flows play a significant part in the evolution of the flow field (Forchheimer, 2016, Anwar, 2008, Liu et al., 2016). It is necessary, therefore, for a FRS simulation tool to address both the complex boundary geometries and the multiple accelerating elements present in the flow field.

Fluid flow in porous media at the field scale is most popularly modeled through finite element, finite volume, and finite difference methods (Aziz and Settari, 1979). To capture the cross flow between the porous rock matrix and the embedded fracture network, these methods incorporate single-porosity, dual-porosity, and discrete fracture models (Zidane and Firoozabadi, 2014, Moortgat and Firoozabadi, 2010, McClure et al., 2016). However, due to the challenges behind the implementation of these methods, and the high computational cost associated with capturing the geometry of the FRS, many in practice choose to idealize the fracture geometry (Mayerhofer et al., 2016, Cipolla et al., 2016, Fuentes-Cruz et al., 2016).

Instead of simulating the FRS within the finite element/volume/difference framework, we propose a different simulation paradigm for the FRS using the lattice Boltzmann method (LBM). The LBM has fundamental properties, which make the method an attractive alternative - including the ability to capture multiple flow regimes of a slightly compressible fluid (Succi, 2001) as well as fine grained system resolution, while maintaining computational efficiency through simple parallelization procedures (Kandhai et al., 2016, Laniewski-Wollk and Rokicki, 2016). Originally developed from the Lattice Gas Automata, the LBM has been successfully applied to fluid flow through porous medium at the pore scale (Succi, 2001). However, sufficient pore geometry information is unavailable at the field scale, and so the LBM was modified to simulate flow over the representative volume element (REV) (Dardis and McCloskey, 1998, Spaid and Phelan, 1997, Freed, 1998).

* Corresponding authors.
E-mail addresses: zbenamram@tamu.edu (Z. Benamram), hadi.nasrabadi@tamu.edu (H. Nasrabadi), egildin@tamu.edu (E. Gildin).

http://dx.doi.org/10.1016/j.advwatres.2016.07.001
0309-1708/

Most recently, Guo and Zhao, (2002) developed a generalized LBM (GLBM) for the simulation of isothermal slightly compressible porous flows at the REV scale. In comparison to previous REV scale LBM, the GLBM includes convective accelerating elements in addition to linear and non-linear damping terms – perfect for the simulation of fluid flow through a FRS.

In this work, we extend the Guo et al. model to the FRS. To fully integrate the GLBM into a reservoir simulation tool, a GLBM FRS is proposed, which addresses the development of boundary conditions along the interface of the fracture network and the surrounding porous media. In addition, the GLBM FRS also provides a derivation of the governing dimensionless equations and a comprehensive methodology for the conversion between the lattice system and the physical system.

The GLBM provides a numerical solution to a slightly compressible fluid governed by a generalized Navier–Stokes equation, which can be applied equally to aquifers or oil reservoirs. The groundwater flow equations presented here have analogs in other fields of study, and so for the purpose of inclusion, this material is generalized to all flows in porous media.

The format of this paper is as follows: an overview of the LBM and the GLBM at the REV scale is given. We then will present the GLBM FRS. All derivations can be found in the appendices. Results for a homogenous and heterogeneous reservoir are presented and validated against a finite difference commercial reservoir simulation software, Eclipse by Schlumberger, (2014). This is the first attempt to verify the GLBM in FRS against commercial reservoir simulation software.

2. The lattice Boltzmann method

2.1. An overview

Two approaches are employed in fluid simulations, commonly classified as bottom-up and top-down. In the top-down approach, the governing macroscopic fluid equations are discretized in time and space (Aziz and Settari, 1979). In the bottom-up approach, individual particles are tracked and their sum behavior represents macroscopic fluid properties. The lattice Boltzmann method is found to exist at a scale neatly between the two. The following section will provide an overview of the LBM. We will begin with the kinetic description of a fluid.

A fluid is characterized as a collection of particles. The LBM treats this particle ensemble as a distribution function. The distribution states the number of particles moving with a specified velocity for all possible velocities. The Maxwell Boltzmann distribution, given by Eq. (1), provides the velocity distribution of a particle ensemble under the condition of point-like, structureless particles,

$$f(u) = \sqrt{\left(\frac{m}{(2\pi KT)}\right)^3} 4\pi u^2 e^{\frac{-mu^2}{2KT}} \tag{1}$$

where f is the particle distribution, u is the velocity, m is the particle mass, and KT is the product of the Boltzmann constant and system temperature (Succi, 2001).

The Maxwell–Boltzmann distribution is both a probability distribution and also a density distribution. This difference in nomenclature arises from whether we apply the distribution to a single particle or a group. In the case of a single particle, the Maxwell-Boltzmann distribution represents the most probable particle speed. For the case of an ensemble, the integral of the distribution function will yield the fluid density, shown in Fig. 1.

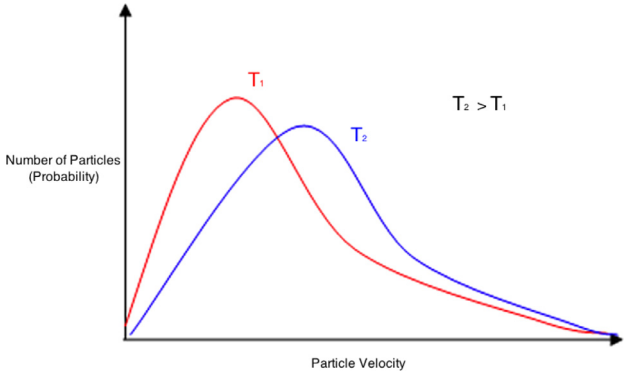

Fig. 1. The Maxwell Boltzmann distribution, where T1 and T2 represent two different system temperatures. The distribution indicates the most probable speed of a particle or the average speed of a fluid group. As the temperature of the system increases, the probability of higher particle velocities increases.

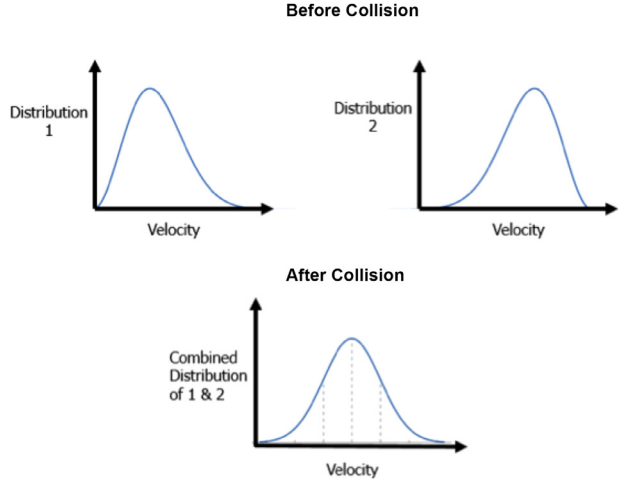

Fig. 2. Two states of a system are pictured, before and after a collision event. Top: in the initial state, two distribution functions are located a distance away, each with a unique density distribution. Bottom: once streaming has completed and the particle ensembles arrive at the same position, collision occurs and the combined distribution relaxes to a state of local equilibrium.

The Boltzmann transport equation, shown in Eq. (2), is the time evolution of the distribution function (Boltzmann, 1964).

$$D_i f = \left[\partial t + \frac{p}{m}\cdot\partial x + F\cdot\partial p\right] f(x,p,t) = \Omega \tag{2}$$

The evolution of the particle ensemble consists of streaming from one location to the next and the collision between other particle ensembles. The left hand side of the transport equation is the streaming step, or the spatial translation of the distribution function, under the influence of an external body force F, where p is the particle momentum. The right hand side shows the effect due to collision between particles, Ω. Collision results in a transfer of momentum, also referred to as a relaxation to local equilibrium (Wolf-Gladrow, 2000). Fig. 2 is a visual representation of these interactions.

So far, we have only considered how particle ensembles move and interact within the continuous regime. However, we cannot compute for infinite degrees of freedom and so for the purposes of numerical simulation, the density distribution function and the Boltzmann transport equation must be discretized.

The process of discretization is shown visually in Fig. 3.

The lattice Boltzmann equation (LBE), shown in Eq. (3) is the first order discretization of the continuous Boltzmann transport

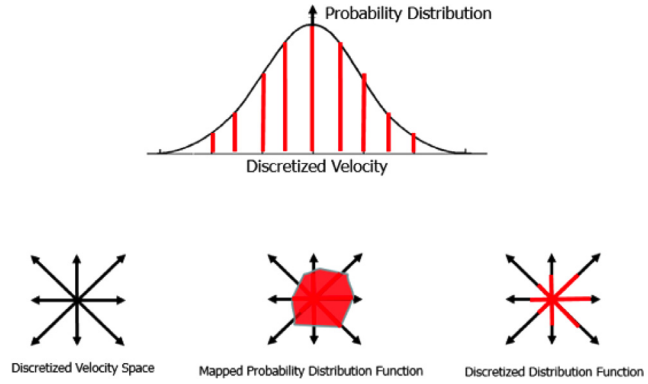

Fig. 3. Top: The continuous Boltzmann distribution is discretized over a finite set of particle velocities. The red lines are the distribution functions associated with a discretized velocity. Bottom: The discretization process occurs over physical space. The volume to be simulated is sectioned into nodes. Each node has a set of velocities, pictured above as the discretized velocity space – D2Q9 (dimension 2, velocity 9). The continuous particle distribution (red) is mapped over the 2-dimensional velocity space to form a lattice distribution. (For interpretation of the references to colour in this figure legend, the reader is referred to the web version of this article.)

equation.

$$f_i(x+e_i\delta_t, t+\delta_t) = f_i(x,t) - \frac{f_i(x,t) - f_i^{eq}(x,t)}{\tau} \tag{3}$$

Here, the collision term Ω is approximated through a BGK operator (Bhatnagar et al., 1954). This approximation states that the rate at which the streamed distribution function relaxes towards local equilibrium is governed by the relaxation parameter τ. The subscript i indicates the direction associated with the D2Q9 lattice (Succi, 2001).

Next, the equilibrium distribution function is discretized over velocity space, given by Eq. (4),

$$f_i^{eq} = w_i\rho\left[1 + \frac{e_i\cdot\mathbf{u}}{c_s^2} + \frac{\mathbf{uu}:\left(\mathbf{e}_i\mathbf{e}_i - c_s^2\mathbf{I}\right)}{2c_s^4}\right] \tag{4}$$

where c_s is the speed of sound of the lattice and defined as $c_s = \frac{\delta x}{\delta t}\frac{1}{\sqrt{3}}$. Lattice velocities e_i and lattice weights w_i are chosen in accordance with the D2Q9 model, and given by Eqs. (5) and (6).

$$e_i = \begin{cases} 0 & i = 0 \\ \left(\cos\left(\frac{\pi}{2}(i-1)\right), \sin\left(\frac{\pi}{2}(i-1)\right)\right) & i = 1\ldots4 \\ \sqrt{2}\left(\cos\left(\frac{\pi}{4}+\frac{\pi}{2}(i-5)\right), \sin\left(\frac{\pi}{4}+\frac{\pi}{2}(i-5)\right)\right) & i = 5\ldots8 \end{cases} \tag{5}$$

$$w_i = \begin{cases} \frac{4}{9} & i = 0 \\ \frac{1}{9} & i = 1\ldots4 \\ \frac{1}{36} & i = 5\ldots8 \end{cases} \tag{6}$$

The volume averaged density and volume averaged velocity are calculated through Eq. (7).

$$\rho = \sum f_i, \text{ and } \rho\mathbf{u} = \sum e_i f_i \tag{7}$$

Through the Chapman–Enskog expansion, an unmodified LBE retains the Navier–Stokes Equation, given by Eq. (8), in the near-incompressible limit (Chapman and Cowling, 1960).

$$\frac{\partial(\rho\mathbf{u})}{\partial t} + \nabla\cdot(\rho\mathbf{uu}) = -\nabla P + \nabla\cdot(\rho\nu_e(\mathbf{u}\nabla + \nabla\mathbf{u})) \tag{8}$$

where P is the fluid pressure and ν_e is the effective kinematic viscosity corresponding to the viscous stress that exists within the fluid itself (as opposed to kinematic viscosity ν, which relates to the viscous stress near solid-liquid interfaces). We can group this equation into accelerating elements. The left hand side of Eq. (8) is the inertial element. The right hand side consists of the pressure and viscous elements.

In summary, fluid is treated as a statistical ensemble of point like particles, the time evolution of which is governed by a series of streaming and collision steps. Although many assumptions have been made in this kinetic description, it is proven in the macroscopic near-incompressible limit that the LBE retains the incompressible Navier–Stokes solution.

2.2. The generalized lattice Boltzmann model

Soon after its emergence, the LBE was successfully applied to fluid flow at pore scales (Succi et al., 1989). A primary advantage of the method is to simulate complex porous geometries without generating a complex lattice mesh. By adding more nodes within the same volume, the resolution of the boundary between solid and fluid nodes is enhanced. This benefit, coupled with a simple parallelization procedure of the LB algorithm, allows for the fast and accurate simulation of fluid flow through a complex geometry (Punzo et al., 1994).

However, a detailed description of the pore geometry is unavailable over a large flow domain. Based on currently available measurement tools, only volume averaged rock properties (permeability and porosity) are obtainable. The representative volume element (REV) is the spatial extent over which this upscaling occurs (Nordahl and Ringrose, 2008). Therefore, the Navier–Stokes equation is generalized to include empirically derived damping forces, which are a function of these volume averaged rock properties. Eqs. (9) and (10) reflect the resistance to flow due the presence of porous medium.

$$\frac{\partial(\rho\mathbf{u})}{\partial t} + \nabla\cdot\left(\frac{\rho\mathbf{uu}}{\phi}\right) = -\nabla P + \nabla\cdot(\rho\nu_e(\mathbf{u}\nabla + \nabla\mathbf{u})) + \rho\mathbf{F} \tag{9}$$

$$\mathbf{F} = -\frac{\phi\nu}{K}\mathbf{u} - \frac{\phi F_e}{\sqrt{\mathbf{K}}}|\mathbf{u}|\mathbf{u} + \phi\mathbf{G} \tag{10}$$

where F is the damping term, K is the permeability, ν is the fluid viscosity due to sheer between fluid and solid boundaries, and ϕ is the rock porosity. F includes the linear in velocity Darcy term, the non-linear in velocity Forchheimer term and an external body force G. As $\phi \to 1$ in the absence of porous media, the generalized Navier–Stokes equation reverts to the Navier–Stokes equation. At low flow velocities, the generalized Navier–Stokes equation reduces to Darcy flow, shown in Eq. (11).

$$\frac{\phi\nu}{K}\mathbf{u} = -\nabla P \tag{11}$$

Significant variations of permeability and porosity over small distances require that the REV be treated as small as possible. Natural and induced fractures add another layer of complexity in modeling flow. Fracture geometries require high spatial resolution. A generalized LBM developed for the simulation of a slightly compressible fluid through porous media at REV scale is uniquely suited to incorporate these complexities.

Several LB models have been developed to simulate fluid flow through porous medium at the REV scale (Dardis and McCloskey, 1998, Spaid and Phelan, 1997, Freed, 1998). Selection of an optimal model should incorporate all relevant flow mechanisms, which govern fluid flow in a highly heterogeneous medium.

Within the LB framework, Guo and Zhao, (2002) proved through the Champman–Enskog expansion that the generalized

Navier–Stokes equation can be obtained from a generalized lattice Boltzmann model (GLBM). To represent the presence of porous medium at every lattice node, the LBE is expanded to include a damping term, which is a function of the volume averaged permeability and porosity shown in Eqs. (12) and (13).

$$f_i(x+e_i\delta_t, t+\delta_t) = f_i(x,t) - \frac{f_i(x,t) - f_i^{eq}(x,t)}{\tau} + \delta_t F_i \tag{12}$$

$$F_i = w_i\rho\left(1-\frac{1}{2\tau}\right)\left[\frac{\mathbf{e}_i\cdot\mathbf{F}}{c_s^2} + \frac{\mathbf{uF}:\left(\mathbf{e}_i\mathbf{e}_i - c_s^2\mathbf{I}\right)}{\phi c_s^4}\right] \tag{13}$$

where the particle distribution functions f_i are treated as equilibrium distribution functions under the assumption of small deviation from local equilibrium (Succi, 2001). **F** is the hydrodynamic damping force shown in Eq. (10). The discretized density distribution function is also altered to reflect the presence of a porous medium shown in Eq. (14).

$$f_i^{eq} = w_i\rho\left[1 + \frac{\mathbf{e}_i\cdot\mathbf{u}}{c_s^2} + \frac{\mathbf{uu}:\left(\mathbf{e}_i\mathbf{e}_i - c_s^2\mathbf{I}\right)}{2\phi c_s^4}\right] \tag{14}$$

The equilibrium distribution function and the forcing term within the generalized LBE are both a function of the macroscopic fluid velocity. To solve for this unknown, the fluid velocity is defined by Eq. (15).

$$\rho\mathbf{u} = \sum e_i f_i + \frac{\delta_t}{2}\rho\mathbf{F} \tag{15}$$

F is also a function of **u** and so Eq. (15) is non-linear with respect to velocity. Since the macroscopic velocity is quadratic, Eq. (15) can be re-written as Eq. (16).

$$\mathbf{u} = \frac{\mathbf{v}}{c_0 + \sqrt{c_0^2 + c_1|\mathbf{v}|}} \tag{16}$$

where **v** is termed the temporal velocity and defined in Eq. 17.

$$\rho\mathbf{v} = \sum e_i f_i + \frac{\delta_t}{2}\phi\rho\mathbf{G} \tag{17}$$

c_0 and c_1 are shown in Eqs. (18) and (19).

$$c_0 = \frac{1}{2}\left[1 + \phi\frac{\delta_t}{2}\frac{\nu}{K}\right] \tag{18}$$

$$c_1 = \phi\frac{\delta_t}{2}\frac{F_e}{\sqrt{K}} \tag{19}$$

The local density computation is identical to the unmodified LBM, where lattice density is equivalent to the summation of individual density distribution functions. In a supplementary article Guo et al. (2002) shows how the governing macroscopic equations are retained through the Chapman–Enskog expansion in the near-incompressible limit. Through this analysis, equations of state are developed, shown in Eq. (20).

$$P = \frac{c_s^2\rho}{\phi} \text{ and } \nu_e = c_s^2\left(\tau - \frac{1}{2}\right)\delta_t \tag{20}$$

3. LBM in a fractured reservoir system

The following two sections will provide the reader with a comprehensive methodology for applying the GLBM (Guo et al., 2002) towards the fractured reservoir system (FRS). Along with the GLBM itself, we must also consider the boundary conditions between the fracture network system and the porous media. In addition a consistent method for converting between the lattice system and the physical system must be established.

3.1. Lattice to physical system conversions: dynamic similarity

For two systems of different scales to exhibit identical flow evolutions, dynamic similarity must exist. Dynamic similarity ensures that two systems have identical length scale, time scale, and force scale ratios (Wolowicz et al., 1979).

We will consider two geometries – the well and fracture. For the lattice system and physical system to exhibit geometric similarity, all three spatial dimension ratios of the reservoir as well as the ratio of well and fracture length to reservoir length must be identical.

A means to measure time scale and force scale ratios is by the non-dimensionalization of the generalized Navier–Stokes equation, through which the relative magnitudes of each force are compared. To derive the non-dimensional form of the generalized Navier Stokes equation, all flow dependent variables are substituted for a linear combination of the associated nondimensional variables and characteristic system variables. A set of characteristic system parameters provide a constant measure of conversion between the physical and dimensionless systems.Typically, boundary conditions inform which parameters are suitable.

The characteristic length $r_{0,p}$ is the physical distance from the inner boundary (well and fracture) to the edge of the reservoir. A second choice for the characteristic length is the node to node distance, or the resolution of the lattice, in physical units. The characteristic time $t_{0,p}$ is chosen to be the fastest time scale for which a fluid can travel the characteristic length. This time scale occurs when the well is opened to production and exhibits the highest flow velocities, providing a bright line measurement for the characteristic velocity $u_{0,p}$. The characteristic time $t_{0,p}$ can also be chosen for the time over which a boundary condition changes. The physical variables, r_p, t_p, and u_p are listed in their dimensionless form as represented in Eq. (21).

$$r_d = \frac{r_p}{r_{0,p}},\ t_d = \frac{t_p}{t_{0,p}},\ u_d = \frac{u_p}{u_{0,p}} \tag{21}$$

Eq. (22) completes the set of dimensionless variables required for the nondimensionalization of the generalized Navier–Stokes equation.

$$\nabla_d = r_{0,p}\nabla_p,\ \nabla_d^2 = r_{0,p}^2\nabla_p^2,\ P_d = \frac{P_p}{\mu_e\frac{u_{0,p}}{r_{0,p}}} \tag{22}$$

where the physical pressure is nondimensionalized by a characteristic viscous sheer stress. The governing flow equation to be made dimensionless is an alternate form of the generalized Navier–Stokes equation, shown in Eq. (23), where only the Darcy term within the damping force is considered.

$$\frac{\partial\mathbf{u}}{\partial t} + \nabla\cdot\left(\frac{\mathbf{uu}}{\phi}\right) = -\frac{1}{\rho}\nabla P + \nu_e\nabla^2\mathbf{u} - \frac{\phi\nu}{K}\mathbf{u} \tag{23}$$

Eq. (23) shows five forcing elements: the time dependent term (variation), convection, pressure, diffusion, and damping in the order that they appear. A dimensionless form of the governing equation, shown in Eq. (24), is obtained by substituting the dimensionless variables found in Eqs. (21) and (22). The full derivation can be found in Appendix A.

$$\frac{Re}{St}\frac{\partial u_d}{\partial t_d} + Re\nabla_d\cdot\frac{u_d u_d}{\phi} = -\nabla_d P_d + \nabla_d^2 u_d - \frac{\phi}{J\,Da}u_d \tag{24}$$

$$Re = \frac{u_{0,p}r_{0,p}}{\upsilon_e},\ J = \frac{\nu_e}{\nu},\ Da = \frac{K}{r_{0,p}^2} \tag{25}$$

$$\phi = \frac{pore\ volume}{total\ volume},\ St = \frac{t_{0,p}\,u_{0,p}}{r_{0,p}} \tag{26}$$

The final non-dimensionalized formulation shows that the evolution of the flow field is government by five dimensionless parameters - the Reynolds number *Re*, the Viscosity ratio *J*, the Darcy number *Da*, porosity ϕ, and the Strouhal number *St*.

In proposing the GLBM, Guo et al. mentioned only four nondimensional parameters governing the evolution of the flow. Shown in the non-dimensional form of the generalized Navier–Stokes equation above, the Strouhal number is also a necessary component when considering the equivalency between physical and lattice systems. The Strouhal number is the ratio of the characteristic flow time scale, $r_{0,p}/u_{0,p}$, normalized by the reference time, $t_{0,p}$. If boundary conditions are changing quickly compared to the flow itself, which can be the case if the bottom-hole pressure rapidly drops, then the Strouhal number will highlight the difference in magnitude between the convective term and the temporal terms. For the purposes of the simulations posed in this paper, the boundary conditions are constant. Therefore, the Strouhal number will be at unity.

To simulate Darcy flow, a choice in parameters must be made such that the magnitude of the Reynolds number is negligible, the Strouhal number is at unity and the combination of the Viscosity ratio and the Darcy number minimized. Under these conditions, the non-dimensionalized governing equation given in Eq. (24) reduces to the dimensionless Darcy equation, shown in Eq. (27).

$$\frac{\phi}{J\,Da}u_d = -\nabla_d P_d \tag{27}$$

We have determined a set of dimensionless parameters, which govern fluid flow evolution by nondimensionalizing the momentum balance equation. Let us apply the same technique to the continuity equation given by Eq. (28) for the case of a near-incompressible fluid with no sinks or sources.

$$\frac{\partial}{\partial t}(\rho\phi) = -\nabla\cdot(\rho u) \tag{28}$$

Eq. (29) is the dimensionless form of Eq. (28). The derivation can be found in Appendix B.

$$\frac{\partial}{\partial t_d}\rho_d = -\frac{1}{\phi}Da\;St\cdot{\nabla_d}^2(P_d) \tag{29}$$

The rate at which density changes over the flow field is proportional to the combined magnitude of the porosity, Darcy and the Strouhal number. This dimensionless grouping allows for a scaling of the characteristic time step. Any scale up to the characteristic time can be absorbed into the permeability term.

To conclude the discussion on dimensionless numbers, a mesoscopic description of a fluid can simulate identical flow evolutions to a system several orders of magnitude in size larger by ensuring that the ratio of forces acting on a volume of fluid is identical and dynamic similarity is maintained. Dimensionless numbers are the measure by which we ensure this similarity.

3.2. Well and fracture boundary conditions

Although high variations in permeability and porosity require the node to node length be minimized, the dimensions of the well and fracture are often smaller than the imposed unit node length. Therefore, it is often necessary to treat system boundaries with as few lattice nodes as possible. However, to retain the governing macroscopic flow equations through the Chapman–Enskog expansion, there must be suffcient node resolution to distinguish between the hydrodynamic and kinetic regimes (Chapman and Cowling, 1960). The Chapman–Enskog analysis depends on the expansion through the smallness parameter, which is the ratio between the kinetic mean-free-path length and the hydrodynamic (smallest macroscopic) length. When the LBE simulates fluid flow over a few lattice nodes, there is no separation between the kinetic and hydrodynamic scales, calling the method's validity into question (Lallemand and Luo, 2000).

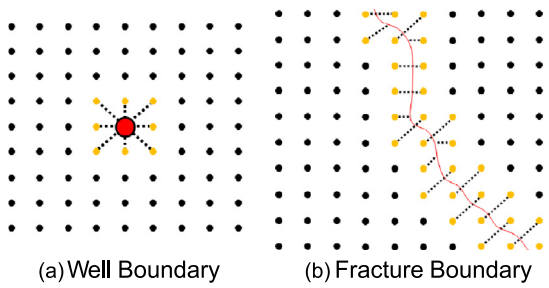

Fig. 4. Pressure is interpolated from the boundary (red) to the nearest neighboring lattice nodes (yellow) at each time step. At these neighboring nodes, the density distribution functions are solved using a modified Zou–He boundary condition. (For interpretation of the references to colour in this figure legend, the reader is referred to the web version of this article.)

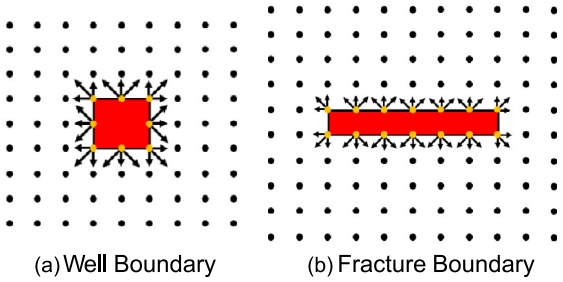

Fig. 5. The area pictured in red is the non-computational regime wherein the boundary lies. The yellow nodes are the nearest neighboring nodes to the boundary. The arrows represent the distribution components that stream from areas not within the computational regime. These distributions are solved through a modified Zou–He boundary condition. (For interpretation of the references to colour in this figure legend, the reader is referred to the web version of this article.)

A low resolution boundary of the well and fracture boundary is achievable, however, through a combination of the damping term inherent to the GLBM and a modified Zou–He boundary condition applied to the well and fracture system. This section will contain the derivation and the procedure to apply a modified Zou–He boundary.

First, to establish the geometry of a constant pressure well and linear fracture, the boundary nodes should be set upon the nearest neighboring nodes of the boundary. In this way, the size of the well and the width of the fracture is incorporated. Pressure is interpolated linearly between the boundary and the nearest neighboring nodes extending radially from the boundary, as shown in Fig. 4.

From the interpolated pressure, the lattice neighboring node density is calculated through an equation of state, given by Eq. (20). The interpolated density is used to solve for the unknown density distribution functions (Zou and He, 2016).

Pictured in Fig. 5 is the area in which the well and fracture boundary lies. On the face of these boundaries, a direct application of the Zo–He boundary condition will yield all unknown distributions that are in the direction of fluid flux. At the corner nodes of the fracture boundary, the flux is neither normal nor parallel to the containing boundary surfaces and therefore the Zou–He boundary must be modified to capture the distribution functions which are in the true direction of fluid flux.

As an example calculation, consider the bottom left corner node of the fracture in Fig. 5b. The unknown distribution functions, f_3,

f_4, and f_7 are calculated in Eqs. 30–32:

$$f_3 = f_1 + \frac{2}{5}(\rho - (f_0 + f_6 + f_8 + 2(f_1 + f_2 + f_5))) + 2(f_6 - f_8) \tag{30}$$

$$f_4 = f_2 + \frac{2}{5}(\rho - (f_0 + f_6 + f_8 + 2(f_1 + f_2 + f_5))) + 2(f_8 - f_6) \tag{31}$$

$$f_7 = f_5 + \frac{1}{5}(\rho - (f_0 + f_6 + f_8 + 2(f_1 + f_2 + f_5))) \tag{32}$$

The full derivation is found in Appendix C. We can apply the modified Zou–He boundary to the well for a more robust treatment of the unknown distribution functions of the well boundary.

To summarize, minimal node usage of the inner boundary is likely in the case of a sparse grid lattice configuration. There have been concerns over low resolution boundaries not respecting the Chapman–Enskog assumptions. In addition, low resolution boundaries can pose problems including the development of lattice effects (flow evolutions that are a result of the underlying grid geometry) (Succi, 2001). A modified Zou–He boundary condition is established to counteract unrealistic flow evolutions and provide stable and accurate simulation results.

3.3. Reservoir edge boundary conditions

Two outer boundary conditions are considered in reservoir simulation: the no-flow boundary condition and the constant pressure boundary condition. The no-flow boundary condition simulates a volumetric reservoir (no external sources of flow on the outer boundary). The constant pressure boundary simulates a reservoir that is bounded by another aquifer system.

Within the LB framework, a direct application of the Zou–He boundary condition on these outer nodes is sufficient. For the simulations posed in this paper, a no-flow boundary condition is used.

4. Results

4.1. Homogenous simulation

The homogenous simulation inputs for the well and the fracture for both the LBM and commercial simulation are as follows: The reservoir is segmented into a 2D array of 200×200 nodes/grid blocks. The node to node distance (or length of the grid block) is 1 m.

The fluid is treated as slightly compressible and the reservoir is fully saturated. Rock compressibility is omitted. The permeability $K = 1$ darcy and porosity ϕ is set at 20%.

The diameter of the well is 0.2 m set directly upon the center node. The fracture is treated as a line source positioned equidistantly from the surrounding nodes. Three fracture lengths are considered for simulation – 80 m, 120 m, and 160 m.

The initial pressure of the reservoir is 100 kPA and the bottomhole flowing pressure is set to be 95% of the initial reservoir pressure. The inner boundary is treated as a constant pressure boundary and the edge of the reservoir maintains a no flow boundary condition. Refer to section: lattice to physical system. Conversions: Dynamic Similarity for converting physical parameters into lattice parameters.

Figs. 6 and 7 show the simulation results for a constant pressure well and fracture producing from a homogenous reservoir. These results are compared against the commercial simulation runs. For both the well and fracture simulations, the results are in excellent agreement for the case of Darcy flow.

We have also compared the GLBM of a linear fracture of various lengths with the Joshi model (Joshi, 1988). The simulation ran under identical conditions as the homogenous simulations presented within this section, aside from a constant pressure boundary condition applied to the reservoir outer boundary. The Joshi model provides an analytical solution for horizontal well flow, but the same solution can be extended to that of a linear fracture. The mode of comparison is the productivity coefficient. The productivity coefficient is calculated as the ratio between the flow rate to the pressure difference at steady state conditions. Results show excellent agreement at small fracture lengths. However, a divergence between the analytical Joshi model and the GLBM develops at larger fracture lengths. This divergence is attributed to the inner boundary approaching the limits of the reservoir (Fig. 8).

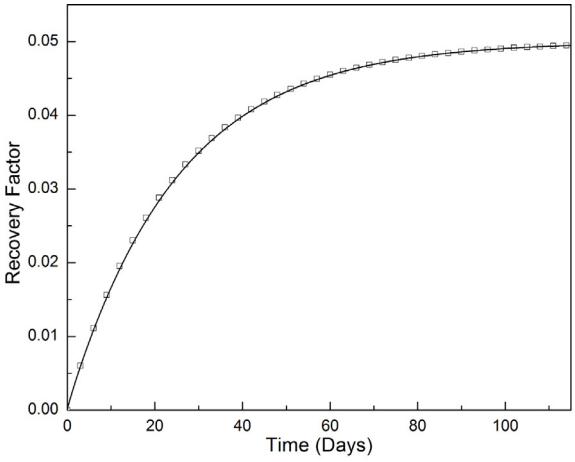

(a) Homogenous well result comparisons

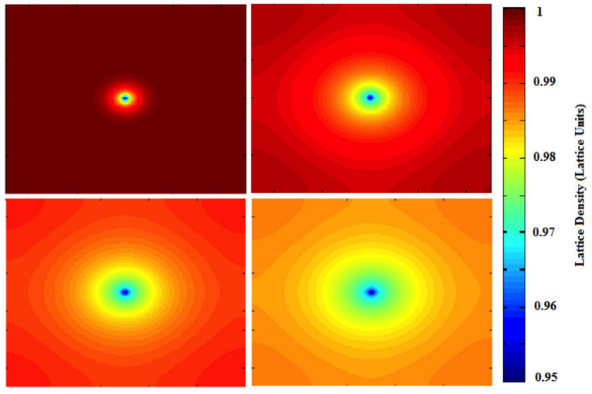

(b) Homogenous well pressure profile

Fig. 6. Simulation of homogenous well reservoir in Darcy flow. Top: comparison plot between generalized LBM (line) and commercial simulation software (box). Bottom: visualized pressure profile of well through production life of reservoir. Pressure measured in lattice units.

4.2. Heterogeneous simulation

The heterogeneous simulation inputs for the well and the fracture for both the LBM and commercial simulation are as follows: The reservoir is segmented into a 2D array of 220×60 nodes/grid blocks. The node to node distance (length of the grid block) is 3 m.

The fluid is treated as slightly compressible and the reservoir is fully saturated. Rock compressibility is omitted. The permeability and porosity arrays are taken from the 10th layer of the SPE-10 collaborative solution project, shown in Fig. D.1 in the Appendix (Spe comparative solution project 2001). The largest permeability value in the array is 2 Darcy and the minimum is $3.8 * 10^{-6}$ Darcy.

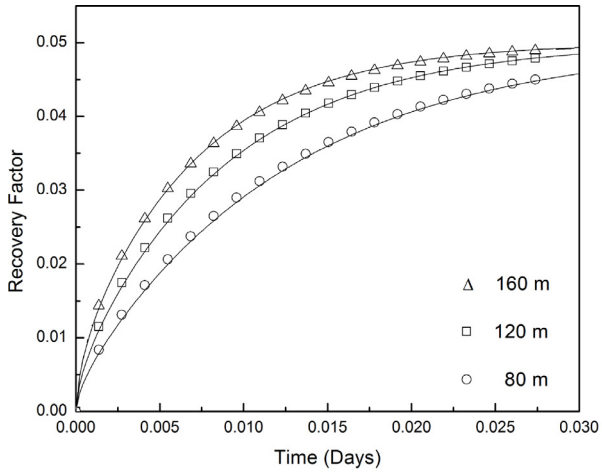

(a) Homogenous fracture result comparisons

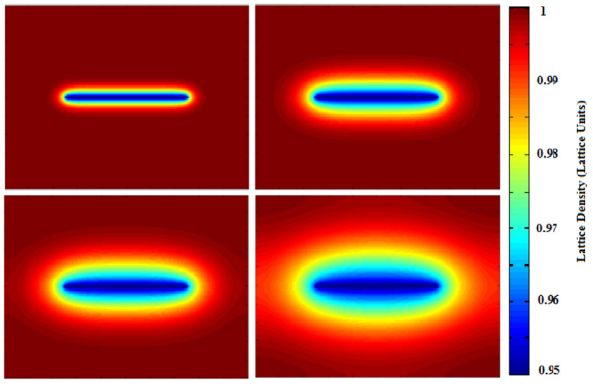

(b) Homogenous fracture pressure profile

Fig. 7. Simulation of homogenous linear fracture reservoir in Darcy flow. Top: comparison plot of three fracture lengths (80 m, 120 m, 160 m) between generalized LBM (line) and commercial simulation software (box). Bottom: visualized pressure profile of linear fracture through production life of reservoir. Pressure measured in lattice units.

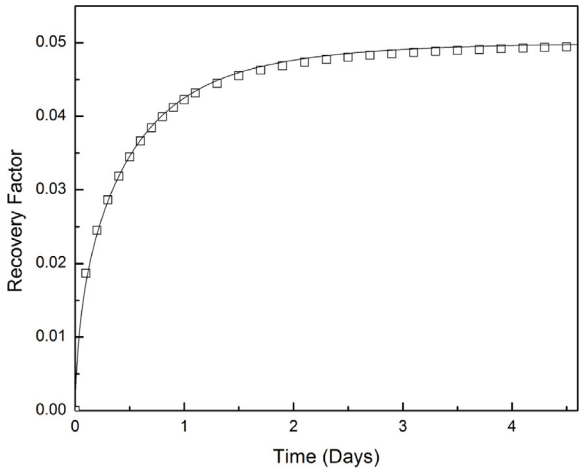

(a) Heterogenous well result comparison

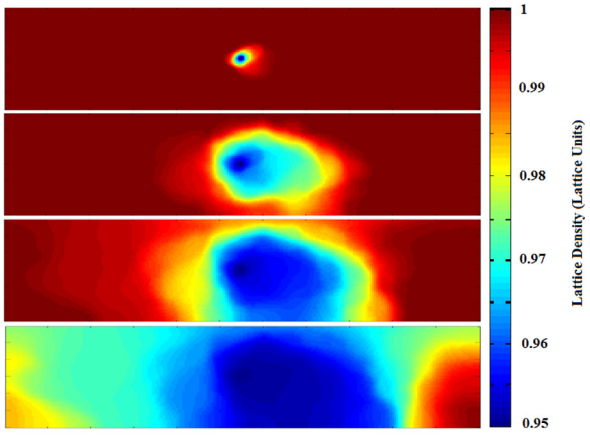

(b) Heterogenous well pressure profile

Fig. 9. Simulation of heterogeneous well reservoir in Darcy flow. Top: comparison plot between generalized LBM (line) and commercial simulation software (box). Bottom: visualized pressure profile of well in heterogeneous medium through production life of reservoir. Pressure measured in lattice units.

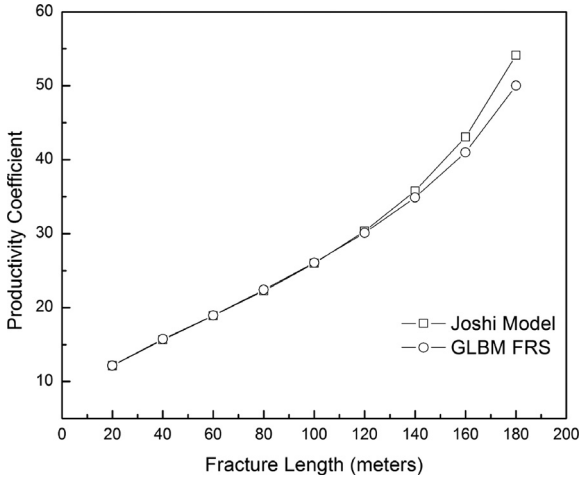

Fig. 8. Comparison of GLBM simulation of linear fracture with Joshi formula for various fracture lengths. Productivity coefficient is calculated as the ratio between flow rate and pressure difference between linear fracture and surrounding reservoir. Divergence from analytical solution is due to fracture approaching boundary of reservoir.

The maximum porosity value is 48% and the minimum is 0%. However, the generalized equilibrium distribution function, given in Eq. (14), cannot take porosity values of 0%. Therefore, all null values of porosity are treated as 10^{-6}%.

For well simulations, the diameter of the well is 0.2 m set in the center of the reservoir. For fracture simulations, the fracture width is treated as a line source and is centrally positioned. Three fracture lengths are considered for simulation −80 m, 120 m, and 160 m.

The initial pressure of the reservoir is 100 kPA and the bottom-hole flowing pressure is set to be 95% of the initial reservoir pressure. The inner boundary is treated as a constant pressure boundary and the edge of the reservoir maintains a no flow boundary condition. Refer to the methodology section for physical to lattice conversion methodology.

Figs. 9 and 10 show the results for the simulation of fluid flow in a heterogeneous porous material under production from a constant pressure well and fracture. The LBM results are compared against the commercial simulation results and show excellent agreement for both cases.

The GLBM FRS simulation shows excellent agreement in the recovery factor over the life of the reservoir for both homogenous and heterogeneous cases. The agreement in simulation results sup-

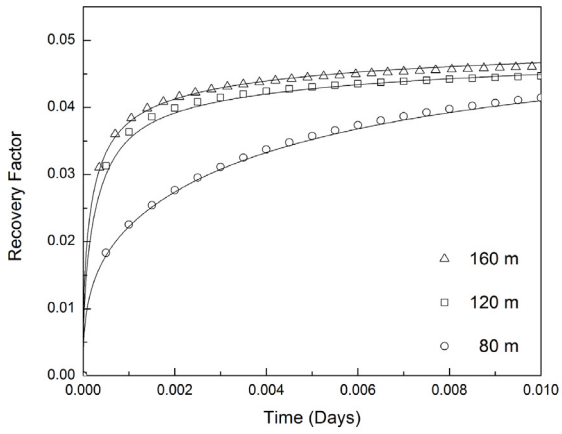

(a) Heterogenous fracture result comparison

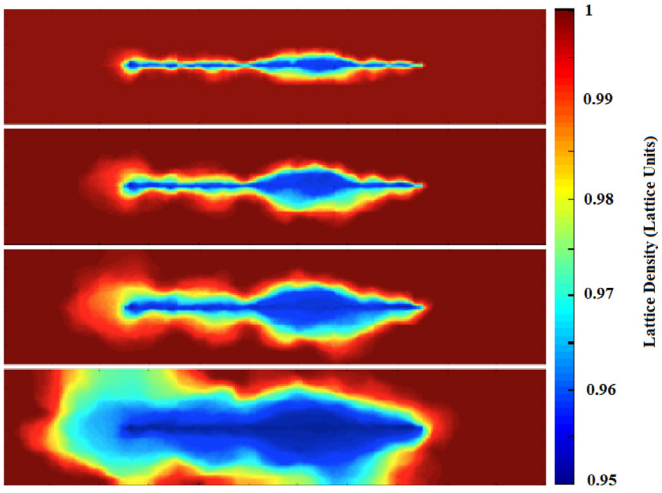

(b) Heterogenous fracture pressure profile

Fig. 10. Simulation of heterogeneous linear fracture reservoir in Darcy flow. Top: comparison plot of three fracture lengths (80 m, 120 m, 160 m) between generalized LBM (line) and commercial simulation software (box). Bottom: visualized pressure profile of linear fracture in heterogeneous medium through production life of reservoir. Pressure measured in lattice units.

ports the use of a modified Zou–He boundary condition for corner nodes of the well and linear fracture.

5. Conclusion

To summarize this work, we have shown that the lattice Boltzmann method can be accurately applied to the case of porous media flows at the REV scale within a fracture network environment. To do so, the original lattice Boltzmann method is extended through the Guo et al. method to incorporate damping terms present within the flow field due to the presence of porous media. A modified Zou–He boundary condition is then developed to model the interface between the well and fracture system with the surrounding porous media. The treatment of the boundary is important because the largest pressure drop exists immediately around the wellbore and fracture system and therefore the majority of the producible fluid is in this region. Lastly, a system of non-dimensional governing equations are derived for the case of the FRS such that the conversion between the lattice and physical system is consistent.

We present results for a homogenous and heterogeneous porous system for the geometries of a well and linear fracture and compare our results with commercial simulation software suites for the case of Darcy flow. Results are in excellent agreement with analytical and finite-difference solutions.

The choice in using a lattice Boltzmann based reservoir simulation tool over other CFD techniques is often viewed as a matter of economics. The LBM can capture a wide range of flow regimes in highly disordered porous media at the REV scale with minimal cost associated with implementation - in other words, the LBM is very easy to implement. Not only is the underlying algorithm simple, but if one chooses a parallel implementation of the codebase for cases of simulating fine grained heterogeneities and complex fracture geometries, it is quick to develop.

In future work, a more complex fracture network will be simulated over multiple flow regimes. Our intention is to examine the differences in production that result from assuming alternative flow regimes and whether these elements make significant contributions to the evolution of the flow field. In addition, rock compressibility will be considered for high pressure reservoirs. Lastly, an analysis of the parallel LBM algorithm will be performed to be compare with other prominent CFD techniques for porous media flows.

Acknowledgments

The support of the member companies of The Crisman Institute of Petroleum Research is gratefully acknowledged.

Appendix A. Non dimensionalization of generalized Navier Stokes

Eqs. (A.1) and (A.2) represent the set of non-dimensional system parameters used in the non-dimensionlization of the governing macroscopic fluid equation, shown in Eq. (A.3). The dimensionless variables are formed through the reference of a characteristic system variable, which can be found in the text of this paper.

$$r_d = \frac{r_p}{r_{0,p}},\ t_d = \frac{t_p}{t_{0,p}},\ u_d = \frac{u_p}{u_{0,p}} \tag{A.1}$$

$$\nabla_d = r_{0,p}\nabla_p,\ \nabla_d^2 = r_{0,p}^2\nabla_p^2,\ P_d = \frac{P_p}{\mu_e \frac{u_{0,p}}{r_{0,p}}} \tag{A.2}$$

$$\frac{\partial \mathbf{u}}{\partial t} + \nabla \cdot \left(\frac{\mathbf{u}\mathbf{u}}{\phi}\right) = -\frac{1}{\rho}\nabla P + \upsilon_e \nabla^2 \mathbf{u} - \frac{\phi \nu}{K}\mathbf{u} \tag{A.3}$$

After substitution of Eqs. (A.1) and (A.2) into Eq. (A.3):

$$\frac{u_{0,p}}{t_{0,p}}\frac{\partial u_d}{\partial t_d} + \frac{u_{0,p}^2}{r_{0,p}}\nabla_d \cdot \frac{u_d u_d}{\phi} = -\frac{\upsilon_e u_{0,p}}{r_{0,p}^2}\nabla_d P_d + \frac{\upsilon_e u_{0,p}}{r_{0,p}^2}\nabla_d^2 u_d - \frac{\nu u_{0,p}}{K}\phi u_d \tag{A.4}$$

Each accelerating element within Eq. (A.4) is composed of a group of characteristic system parameters and a non-dimensional group, which is of the order 1 everywhere within the flow field. The relative magnitudes of these forces (accelerating elements) are dictated by the characteristic system parameter group. These coefficients have units of *length/time*^{2}. We therefore can compare the relative magnitudes of each forcing element to one another to determine the dominating flow regime.

Let us compare the relative magnitude of the viscous force, given by $\upsilon_e u_{0,p}/r_{0,p}^2$ in Eq. (A.4) to all other elements by dividing throughout by the viscous coefficient.

$$\frac{u_{0,p}r_{0,p}}{\upsilon_e}\frac{r_{0,p}}{u_{0,p}t_{0,p}}\frac{\partial u_d}{\partial t_d} + \frac{u_{0,p}r_{0,p}}{\upsilon_e}\nabla_d \cdot \frac{u_d u_d}{\phi} = -\nabla_d P_d + \nabla_d^2 u_d - \phi\frac{\nu}{\upsilon_e}\frac{r_{0,p}^2}{K} \tag{A.5}$$

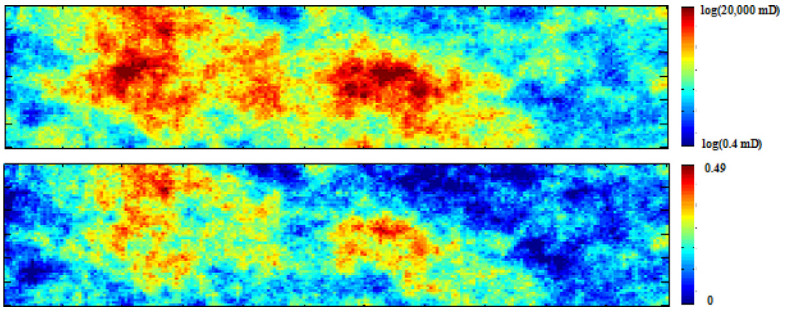

Fig. D.1. SPE-10 permeability (top) and porosity (bottom) data. Permeability values are scaled logarithmically for viewing. SPE-10 data is used to compare the generalized LBM with commercial simulation software. The 10th layer of the permeability and porosity field were used for simulation of 2D reservoir.

$$\frac{Re}{St}\frac{\partial u_d}{\partial t_d} + Re\nabla_d \cdot \frac{u_d u_d}{\phi} = -\nabla_d P_d + \nabla_d^2 u_d - \frac{\phi}{J\,Da} u_d \tag{A.6}$$

$$Re = \frac{u_{0,p} r_{0,p}}{\nu_e},\ J = \frac{\nu_e}{\nu},\ Da = \frac{K}{r_{0,p}^2} \tag{A.7}$$

$$\phi = \frac{pore\ volume}{total\ volume},\ St = \frac{u_{0,p} t_{0,p}}{r_{0,p}} \tag{A.8}$$

Appendix B. Non dimensionalization of the continuity equation

$$\frac{\partial}{\partial t}(\rho\phi) = -\nabla \cdot (\rho u) \tag{B.1}$$

By substituting in the Darcy correlation for fluid velocity in porous media,

$$\frac{\partial}{\partial t}(\rho\phi) = -\nabla \cdot \left(\frac{K}{\nu}(\nabla P)\right) \tag{B.2}$$

Using the variable assignments in A and $\rho_d = \rho_p/\rho_{0,p}$, where $\rho_{0,\,p}$ is a characteristic system density, a simple substitution yields:

$$\frac{\rho_{0,p}}{t_{0,p}}\frac{\partial}{\partial t_d}(\phi\rho_d) = -\frac{K}{\nu}\frac{\mu u_{0,p}}{r_{0,p}}\frac{1}{r_{0,p}^2} \cdot \nabla_d{}^2(P_d) \tag{B.3}$$

By dividing the above equation throughout by the coefficient of the time dependent term, we arrive at the following:

$$\frac{\partial}{\partial t_d}(\phi\rho_d) = -\frac{K}{r_{0,p}^2}\frac{u_{0,p} t_{0,p}}{r_{0,p}} \cdot \nabla_d{}^2(P_d) \tag{B.4}$$

$$\frac{\partial}{\partial t_d}\rho_d = -\frac{1}{\phi} Da\ St \cdot \nabla_d{}^2(P_d) \tag{B.5}$$

Appendix C. Modified Zou–He boundary formulation

We assume that the bounce-back condition is valid for the non-equilibrium part of the distribution functions, given by Eqs. (C.1)–(C.3) (Zou and He, 2016).

$$f_3 = f_1 + f_3^{eq} - f_1^{eq} \tag{C.1}$$

$$f_4 = f_2 + f_4^{eq} - f_2^{eq} \tag{C.2}$$

$$f_7 = f_5 + f_7^{eq} - f_5^{eq} \tag{C.3}$$

If we solve for the equilibrium contributions in Eqs. (C.1)–(C.3) using Eq. (14), Eqs. (C.4)–(C.6) are formed.

$$f_3 = f_1 - \frac{2}{3}\rho u_x \tag{C.4}$$

$$f_4 = f_2 - \frac{2}{3}\rho u_y \tag{C.5}$$

$$f_7 = f_5 - \frac{1}{6}(\rho u_x + \rho u_y) \tag{C.6}$$

By the definition of ρ we have:

$$\rho = f_0 + f_1 + f_2 + f_3 + f_4 + f_5 + f_6 + f_7 + f_8 \tag{C.7}$$

Further substitution of Eqs. (C.4)–(C.6) into Eq. (C.7) leads to Eq. (C.8):

$$\rho u_x + \rho u_y = -\frac{6}{5}(\rho - (f_0 + f_6 + f_8 + 2(f_1 + f_2 + f_5))) \tag{C.8}$$

Next, we will employ the definition of the temporal macroscopic velocity, given by Eq. 17.

$$\rho u_x = f_1 - f_3 + f_5 - f_7 + f_8 - f_6 \tag{C.9}$$

Through the substitution of Eqs. (C.4)–(C.6) into Eq. (C.9), we form Eq. (C.10).

$$\rho u_x - \rho u_y = 6(f_8 - f_6) \tag{C.10}$$

Now, all the relevant information has been derived to solve for f_3, f_4, and f_7. The rearrangement and combination of Eqs. (C.8) and (C.10) yield:

$$f_3 = f_1 + \frac{2}{5}(\rho - (f_0 + f_6 + f_8 + 2(f_1 + f_2 + f_5))) + 2(f_6 - f_8) \tag{C.11}$$

$$f_4 = f_2 + \frac{2}{5}(\rho - (f_0 + f_6 + f_8 + 2(f_1 + f_2 + f_5))) + 2(f_8 - f_6) \tag{C.11}$$

$$f_7 = f_5 + \frac{1}{5}(\rho - (f_0 + f_6 + f_8 + 2(f_1 + f_2 + f_5))) \tag{C.13}$$

Appendix D. SPE-10 permeability and porosity field

Fig. D.1

References

Anwar, S., 2008. Lattice Boltzmann modeling of fluid flow and solute transport in karst aquifers. FIU Ph.D. thesis.

Aziz, K., Settari, A., 1979. Petroleum Reservoir Simulation. Applied Science Publishers Ltd.

Bhatnagar, P.L., Gross, E.P., Krook, M., 1954. A model for collision processes in gases. i. small amplitude processes in charged and neutral one-component systems. Phys. Rev. 94, 511–525. http://dx.doi.org/10.1103/PhysRev.94.511.

Boltzmann, L. 1964. Lectures on Gas Theory, University of California Press.

Chapman, S., Cowling, T.G., 1960. The mathematical theory of non-uniform gases: an account of the kinetic theory of viscosity. thermal condition, and diffusion in gases. Cambridge University Press.
Cipolla, C., Lolon, E., Erdle, J., Rubin, B., 2016. Reservoir modeling in shale-gas reservoirs. SPE J. http://dx.doi.org/10.2118/125530-PA.
Dake, L., 1978. Fundamentals of Reservoir Engineering. Elsevier BV, Amsterdam, The Netherlands.
Dardis, O., McCloskey, J., 1998. Lattice Boltzmann scheme with real numbered solid density for the simulation of flow in porous media. Phys. Rev. E 57, 4834–4837. http://dx.doi.org/10.1103/PhysRevE.57.4834.
Forchheimer, P., 2016. Wasserbewegung durch boden. Zeitschrift des Vereines Deutscher Ingenieuer.
Freed, D.M., 1998. Lattice-Boltzmann method for macroscopic porous media modeling. Int. J. Modern Phys. C 09 (08), 1491–1503. http://dx.doi.org/10.1142/S0129183198001357.
Fuentes-Cruz, G., Gildin, E., Valk, P., 2016. Analyzing production data from hydraulically fractured wells: the concept of induced permeability field. Society of Petroleum Engineers http://dx.doi.org/10.2118/163843-PA.
Guo, Z., Zheng, C., Shi, B., 2002. Discrete lattice effects on the forcing term in the lattice Boltzmann method. Phys. Rev. E 65, 046308. http://dx.doi.org/10.1103/PhysRevE.65.046308.
Guo, Z., Zhao, T., 2002. Lattice Boltzmann model for incompressible flows through porous media. Phys. Rev. E 66. http://dx.doi.org/10.1103/PhysRevE.66.036304.
Joshi, S., 1988. Augmentation of well productivity with slant and horizontal wells. J. Pet. Technol. 729–739.
Kandhai, D., Koponen, A., Hoekstra, A., Kataja, M., Timonen, J., Sloot, P., 2016. Lattice-Boltzmann hydrodynamics on parallel systems. Comput. Phys. Commun. 111. http://dx.doi.org/10.1016/S0010-4655(98)00025-3.
King, G., 2016. Thirty years of gas shale fracturing: what have we learned? Society of Petroleum Engineers http://dx.doi.org/10.2118/133456-MS.
Lallemand, P., Luo, L.-S., 2000. Theory of the lattice Boltzmann method: dispersion, dissipation, isotropy, galilean invariance, and stability. Phys. Rev. E 61, 6546–6562. http://dx.doi.org/10.1103/PhysRevE.61.6546.
Laniewski-Wollk, L., Rokicki, J., 2016. Adjoint lattice Boltzmann for topology optimization on multi-gpu architecture. Comput. Math. Appl. http://dx.doi.org/10.1016/j.camwa.2015.12.043.
Liu, R., Li, B., Jiang, Y., 2016. Critical hydraulic gradient for nonlinear flow through rock fracture networks: the roles of aperture, surface roughness, and number of intersections. Adv. Water Resour. 88, 53–65. http://dx.doi.org/10.1016/j.advwatres.2015.12.002.
Mayerhofer, M., Lolon, E., Youngblood, J., Heinze, J., 2016. Integration of microseismic-fracture-mapping results with numerical fracture network production modeling in the barnett shale. Presented at the SPE Annual Technical Conference and Exhibition, San Antonio, Texas http://dx.doi.org/10.2118/102103-MS.
McClure, M., Babazadeh, M., Shiozawa, S., Huang, J., 2016. Fully coupled hydromechanical simulation of hydraulic fracturing in 3D discrete-fracture networks. SPE J. http://dx.doi.org/10.2118/173354-PA.
Moortgat, J., Firoozabadi, A., 2010. Higher-order compositional modeling with fickian diffusion in unstructured and anisotropic media. Adv. Water Resour. 33 (9), 951–968. http://dx.doi.org/10.1016/j.advwatres.2010.04.012.
Nordahl, K., Ringrose, P.S., 2008. Identifying the representative elementary volume for permeability inheterolithic deposits using numerical rock models. Math. Geosci. 40 (7), 753–771.
Punzo, G., Massaioli, F., Succi, S., 1994. High-resolution lattice-Boltzmann computing on the IBM SP1 scalable parallel computer. Comput. Phys. 8, 705–711. http://dx.doi.org/10.1063/1.168487.
URL Schlumberger. Eclipse.
Spaid, M.A.A., Phelan, F.R., 1997. Lattice boltzmann methods for modeling microscale flow in fibrous porous media. Phys. Fluids 9 (9), 2468–2474.
Spe comparative solution project 2001. URL: http://www.spe.org/web/csp/.
Succi, S., Foti, E., Higuera, F., 1989. Three-dimensional flows in complex geometries with the lattice Boltzmann method. EPL (Europhys. Lett.) 10 (5), 433.
Succi, S., 2001. The Lattice Boltzmann Equation. Oxford University Press.
Warpinski, N., Teufel, L., 2016. Influence of geologic discontinuities on hydraulic fracture propagation. J. Pet. Technol. 39. http://dx.doi.org/10.2118/13224-PA.
Wolf-Gladrow, D.A., 2000. Lattice-Gas Cellular Automata and Lattice Boltzmann Models. Springer-Verlag, Berlin Heidelberg http://dx.doi.org/10.1007/b72010.
Wolowicz, C., Jr., J.B., Gilbert, W., 1979. Similitude requirements and scaling relationships as applied to model testing Tech. rep..
Zidane, A., Firoozabadi, A., 2014. An efficient numerical model for multicomponent compressible flow in fractured porous media. Adv. Water Resour. 74, 127–147. http://dx.doi.org/10.1016/j.advwatres.2014.08.010.
Q. Zou, X. He, On pressure and velocity boundary conditions for the lattice Boltzmann BGK model, American Institute of Physics: Physics of Fluids.2016